ADVANCED FUNCTIONAL MATERIALS
www.afm-journal.de

Template-Assisted Synthesis of π-Conjugated Molecular Organic Nanowires in the Sub-100 nm Regime and Device Implications

*Kazi M. Alam, Abhay P. Singh, Ryan Starko-Bowes, Srikrishna C. Bodepudi, and Sandipan Pramanik**

π-conjugated molecular organics such as rubrene, Alq_3, fullerene, and PCBM have been used extensively over the last few decades in numerous organic electronic devices, including solar cells, thin-film transistors, and large-area, low-cost flexible displays. Rubrene and Alq_3, have emerged as promising platforms for spin-based classical and quantum information processing, which has triggered significant research activity in the relatively new area of organic spintronics. Synthesis of these materials in a nanowire geometry, with feature sizes in the sub-100 nm regime, is desirable as it often enhances device performance and is essential for development of high-density molecular electronic devices. However, fabrication techniques that meet this stringent size constraint are still largely underdeveloped. Here, a novel, versatile, and reagentless method that enables growth of nanowire arrays of the above-mentioned organics in the cylindrical nanopores of anodic aluminum oxide (AAO) templates is demonstrated. This method 1) allows synthesis of high-density organic nanowire arrays on arbitrary substrates, 2) provides electrical access to the nanowire arrays, 3) offers tunability of the array geometry in a range overlapping with the relevant physical length scales of many organic devices, and 4) can potentially be extended to synthesize axially and radially heterostructured organic nanowires. Thus prepared nanowires are characterized extensively with an aim to identify their potential applications in diverse areas such as organic optoelectronics, photovoltaics, molecular nanoelectronics, and spintronics.

1. Introduction

π-conjugated organic semiconductors, which are broadly divided into the classes of macromolecular polymers and small molecular weight compounds, have been studied extensively over the last few decades due to their unconventional attributes such as chemical tunability of optical, electronic and spintronic properties and amenability to roll-to-roll processing which leads to large-area, low-cost printed electronics.[1,2] Nanowires of organic semiconductors are recently attracting increasing interest since this geometry often offers enhanced device performance. For example, in case of organic solar cells, a promising method of improving efficiency is to achieve nanometer scale interpenetrating networks of donor and acceptor materials, with an interfacial distance smaller than the exciton diffusion length (~10–20 nm) in the organic. An ideal configuration that has been proposed for these cells consists of an array of vertically aligned donor organic nanowires attached to an electrode and surrounded by an acceptor type organic connected to another electrode.[3–8] Similarly, electrical properties of organic nanowires can be tuned by varying the nanowire geometry[9] and can potentially be exploited to develop high-performance transistors that rival the performance of amorphous silicon.[10] Finally, another area where organic nanowires have recently emerged as a promising candidate is the relatively new field of "organic spintronics".[11–13] Organic materials, due to their weak spin-orbit and hyperfine interactions offer an attractive platform in which spin memory of a carrier can be preserved for sufficiently long time.[14,15] This makes organics a suitable host for spin-based classical and quantum bits.[14,15] The chemical composition of the organics and molecular packing can be changed to control the strengths of these interactions[16,17] and hence spin lifetime is tunable in such systems. Further, nanowire geometry allows identification of the dominant spin relaxation mode in organics[14] and investigation of spin-phonon coupling,[18] a knowledge of which is a crucial ingredient for room-temperature organic spintronics.[19]

Despite all these potentials, fabrication of organic molecular semiconductors in nanowire shape with controllable geometry and aspect ratio remains a significant challenge. The commonly used techniques include submicron lithography, electrospinning, supramolecular self-assembly in solution and at

K. M. Alam, A. P. Singh, R. Starko-Bowes,
S. C. Bodepudi, S. Pramanik
Department of Electrical and Computer Engineering
University of Alberta
9107-116 Street, ECERF W2-102
Edmonton, AB T6G 2V4, Canada
E-mail: spramani@ualberta.ca

DOI: 10.1002/adfm.201102967

interfaces, physical vapor transport and template assisted synthesis.[20] For the fabrication of high-density arrays of vertically aligned and segmented nanowires, template based approaches appear to be more promising. This method offers tight control over the geometry of the nanowires and inter-nanowire spacing and can be easily integrated with additional fabrication steps to produce functional optical, electronic, optoelectronic and spintronic devices.[21] In this work we use an anodic aluminum oxide (AAO) template for the synthesis of organic molecular nanowires. Compared to polymer track etched membranes, anodic alumina templates offer better pore ordering and higher pore density. Anodic alumina templates also allow wider range of pore length and diameter and higher thermal and mechanical stability compared to soft templates such as block copolymers.

In the past several groups have reported AAO-based synthesis of long chain polymer nanowires. For example, ref. [22,23] synthesized nanorods and nanotubes of poly(p-phenylene vinylene) (PPV) within the pores of AAO template. Polypyrrole (PPy) nanowires have been grown using electropolymerization.[24,25] Arrays of PEDOT nanowires hosted in AAO template have been reported in ref. [26]. Among other polymers that have been grown within AAO are PFO,[27–31] F8T2[30] (solution-assisted template wetting), Poly(3-hexylthiophene),[32] regioregular polythiophene,[33] P3MT[34] (electrochemical polymerization). The work cited above represents a small cross-section of the huge amount of research that has been performed to date on polymer nanowire synthesis in AAO template. For a comprehensive review of this area the reader is directed to ref. [20,35].

Synthesis of small molecular weight organic semiconductors (such as rubrene, Alq_3, C_{60} and PCBM) in AAO templates has received limited success in the past[35] in spite of the huge technological potential of such materials. Ref. [14,19,36,37] performed evaporation of small molecular weight organics within the pores. For small pore diameter (~50 nm), only a very thin layer (~30 nm) of organic can be deposited[14,19,36] within the pore. Prolonged evaporation tends to clog the pores and halts the nanowire growth process (Supporting Information section IV, Figure S2). For longer nanowires it is necessary to employ larger diameter pores (~200 nm),[37] which is unfortunately too wide to provide any significant functional advantage for many device applications and this method therefore does not offer any structural tunability. Ref. [38–40] reported fabrication of fullerene nanowires within the nanopores via a template wetting method. However, in most cases thick commercial templates (~50 μm) with both side open pores and large diameter (~200 nm) were used. Such method has not produced nanowires in one-side closed pores presumably due to the presence of trapped air pockets within the pores (Supporting Information section IV, Figure S1). We note that one-side open pores are more common in device applications where short nanowires are required and hence the template is synthesized on a suitable substrate, which provides necessary mechanical stability to the fragile template. The ability to fabricate nanowires of molecular organics with controllable geometry in sub-100 nm regime would be an important advance since it would offer the potential to exploit the diverse benefits of nanoscale features in various optical, electronic, optoelectronic and spintronic applications where the above-mentioned materials play a pivotal role.

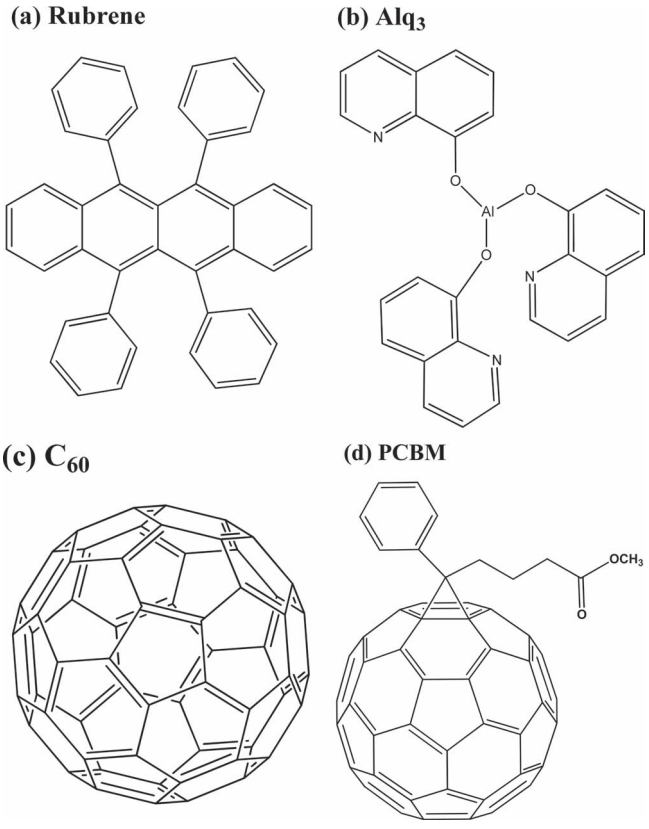

Scheme 1. Chemical structures of the molecular organics considered in this study.

In this work we report synthesis and subsequent characterization of nanowires of four different molecular organics (**Scheme 1**) that are commonly used in organic photovoltaics, light-emitting diodes, transistors and spin valves: (a) rubrene (5,6,11,12-tetraphenylnaphthacene), (b) tris-8 hydroxyquinoline aluminum (Alq_3), (c) fullerene (C_{60}) and (d) PCBM ([6,6]-phenyl-C_{61}-butyric acid methyl ester). The organic nanowires are formed within the cylindrical nanopores (20–80 nm diameter, 1 μm long) of an anodic alumina template by a novel "fixed angle centrifugation assisted growth" method (**Scheme 2**). This process is reagentless, one-step, produces large array of vertically oriented organic nanowires and does not require special apparatus. As we will show below, this method also allows fabrication of axially heterostructured metal-organic bilayer hybrid nanowires, permits direct electrical contact at the two ends of the nanowires and therefore can be used for synthesis of various functional organic nanowire devices.

2. Results and Discussion

2.1. Growth of Organic Nanowire Arrays

Preparation of nanoporous anodic alumina templates has been performed by a well-established two-step anodization process[21] described in the Supporting Information section I. Pore lengths

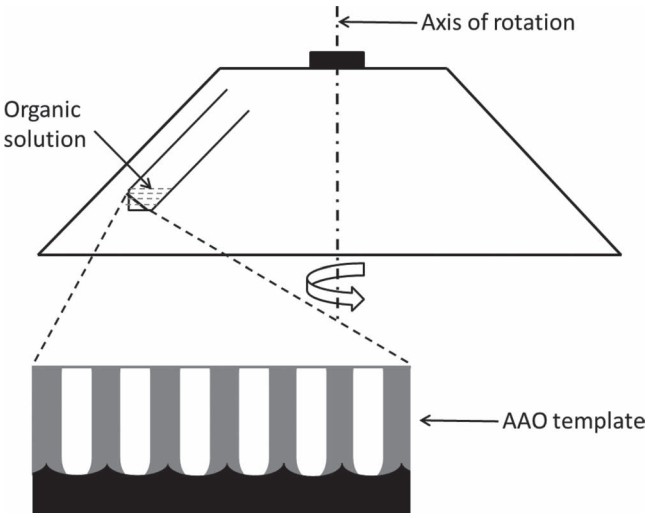

Scheme 2. Illustration of the fixed-angle centrifugation-assisted growth method for growth of molecular organic nanowires. The empty AAO templates are loaded in a standard commercial centrifuge, which is filled with organic solutions. Centrifugation is performed under the conditions specified in the text.

of several hundred nanometers with diameter and interpore spacing tunable in the sub-100 nm range are required for applications in organic photovoltaics and spintronics since for small-molecule organics the relevant length scales (exciton diffusion length and spin relaxation length respectively) are typically in this range.[11,14,41,42] As mentioned before, nanowire conductivity can also be controlled by varying nanowire diameter in sub-100 nm regime.[9] The anodization parameters are therefore tuned to generate array features lying in this size range.

Figure 1a shows field emission scanning electron microscopic (FESEM) images of a pristine (unfilled) oxalic acid anodized AAO template used for synthesizing organic nanowires. In this case, nominal pore diameter is 50 nm, pore length is 1 μm, and wall thickness between neighboring pores is 50 nm. In spite of the short duration of the second step anodization (Supporting Information section I), the pores are straight with no signature of branching (Figure 1a, main image), have narrow size distribution and exhibit a hexagonal ordering (Figure 1a, bottom inset). There exists a uniform alumina barrier layer of thickness 30 nm at the pore bottom (Figure 1a, main image), which needs to be removed for transport experiments. This can be achieved by a pore-side etching technique (Supporting Information section I), which removes the barrier layer with simultaneous widening of the pores (Figure 1a, top inset). For transport characterization, organic nanowires are grown within such pores and the nanowires are therefore in direct contact with the aluminum substrate, which acts as the bottom electrode. It is important to note that this pore growth process can be executed on arbitrary substrates like glass, indium tin oxide (ITO), silicon etc.[43–45] and a recent work has also shown independent control over pore diameter and interpore spacing.[46] Therefore, using the growth mode described in this work it is possible to synthesize organic nanowire arrays with controllable geometry on arbitrary substrates as required by a specific application. In this work we demonstrate the growth method of organic nanowires using aluminum foil as the substrate.

Standard template wetting techniques typically involve placing few drops of the organic solution on the nanoporous template.[25,27,30,35,38–40] The solution enters the pores via capillary action and after evaporation of the solvent, organic material remains inside the nanopores and forms nanowires. As mentioned above, many groups have used this method successfully in the past to fabricate nanowire arrays of long chain polymers. This method, however, is not effective for small molecular weight organic solutions and negligible amount of organic enters the pores, irrespective of pore diameter (see Supporting Information section IV for details).

To drive the organic material within the nanopores we coupled the traditional template wetting technique with a simultaneous fixed angle centrifugation process. The centrifugal force on the solvent thrusts the organic solution within the pores and after evaporation of the solvent, the trapped organic forms nanowire within the cylindrical nanopores. The experimental setup for organic growth is shown in Scheme 2. The nanoporous templates are loaded in the centrifugation tubes and are completely immersed in a saturated solution of the organic (Supporting Information section II). The centrifugation is carried out at 4000 rpm for 5 min. The samples are not removed from the solution prior to the complete evaporation (room temperature) of the organic solvent. The top surface of the template is repeatedly cleaned by the same organic solvent. This cleaning step does not affect the nanowires hosted within the pores. To confirm the penetration of organic within the nanopores we have exposed the nanowire tips from the backside of the template by sequential etching of aluminum and the barrier layer (Supporting Information section III). The cleaned top surface was covered with a sacrificial polymer for mechanical stability of the submicron-thick templates.

Figure 1b shows the oblique cross-sectional FESEM images of the rubrene nanowires synthesized within the template (main image). The nanowire tips are clearly visible from the backside of the template (top insets). Some of these tips have merged together due to prolonged removal of the supporting AAO host matrix (top left inset). The top right inset shows the nanowire tips after short-time etching of alumina from the backside. In this case no merging has occurred. In general, we find that after short time etching of the template, the nanowires match perfectly to the contours of the host anodic alumina template. However, after long time etching, the exposed tips tend to have slightly larger diameter than the nanopores. This "swelling" occurs because during the etching process the aqueous solvents expand the organic nanowires and the expanded shape does not return to its original form even after drying. Similar effect has been reported before in the context of template grown polymer nanowires.[22,24]

Figure 1c shows Alq_3 nanowires grown in 50 nm pores. The nanowires tend to coalesce after removal of the host template. The inset shows the Alq_3 nanowire tips imaged from the backside of the template. Figure 1d shows PCBM nanowires (main image and top inset) and C_{60} nanowires (bottom inset) grown within the anodic alumina template. These materials typically tend to form hollow nanowires with a closed tip at the bottom

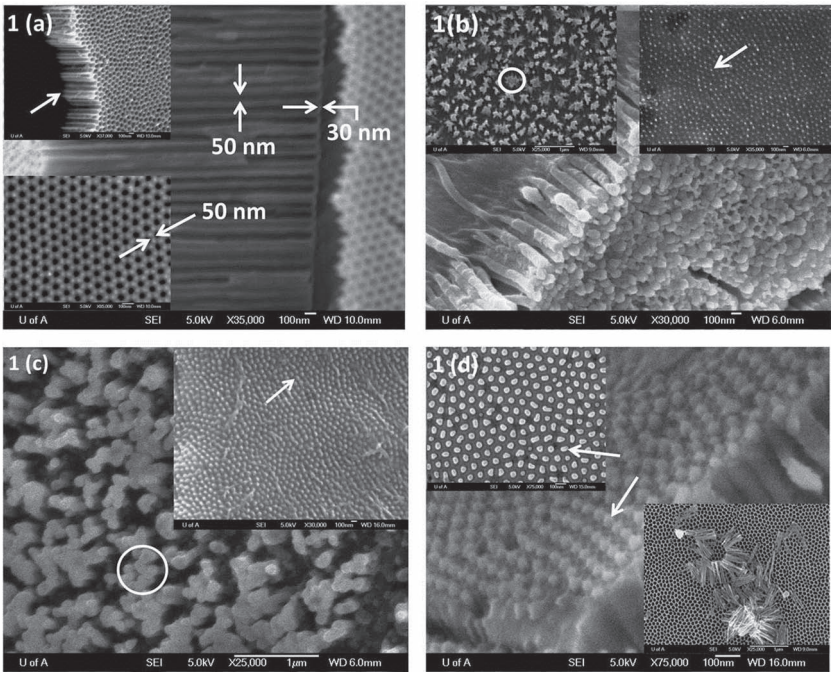

Figure 1. Templated synthesis of molecular organic nanowires. a) (main image) Cross-sectional view of an as-prepared pristine AAO template, synthesized by oxalic acid anodization. The nominal pore diameter is 50 nm. An insulating non-porous barrier layer (30 nm thick) is visible at the pore bottom. (bottom inset) Top view of the template, illustrating hexagonal arrangement of the nanopores. The arrow indicates wall thickness of 50 nm. (top inset) Cross-sectional view of the template after pore-side etching. The arrow indicates removal of the barrier layer. b) (main image) Oblique, cross-sectional view of the rubrene nanowires (70 nm diameters) grown within the AAO template. (top right inset) Rubrene nanowire tips exposed from the backside of the template after slight removal of alumina matrix. (top left inset) Rubrene nanowire tips merge together (shown by circle) after continued removal of the host matrix. c) (main image) Alq_3 nanowire tips exposed from the backside of the template. Wire diameter is 70 nm and some merging (circle) is visible. (top inset) Alq_3 nanowire tips (arrow) after slight removal of the alumina. d) (main image) Oblique view of PCBM nanowire (50 nm diameter) tips exposed from the backside of the template. (top inset) Plan view of the PCBM nanowire tips. (bottom inset) A collection of fullerene (C_{60}) nanowires (50 nm diameter) on the surface of the AAO template. All images were taken using a field emission scanning electron microscope.

(i.e. at the interface with aluminum). This occurs because the centrifugation process thrusts the solution to the pore bottom and therefore high concentration of organic is expected at the pore bottom. In all cases the FESEM images indicate near complete filling of most of the pores and demonstrate the efficiency of this process for high yield production of well-ordered array of vertically oriented organic molecular nanowires.

Figure 2 shows narrower diameter (20 nm) organic nanowires synthesized in sulphuric acid anodized AAO templates. In this case both pore diameter and wall thickness are smaller (~20 nm, inset of Figure 2a) than before. Organic nanowires can still be grown within such narrow pores via the same method described above. Figures 2a (main image) and b show released and bunched nanowires of rubrene and Alq_3 respectively after (near complete) removal of the host AAO matrix.

This method of organic growth can easily be coupled with traditional electrodeposition process to synthesize axially heterostructured metal-organic bilayer nanowires. We first deposit metal at the pore bottom from a slightly acidic solution of an appropriate metal-salt using standard dc (or ac) electrodeposition.[21] Next organic nanowires are grown on top of the metal nanowire segments using the process described above. We note that a wide range of metals (Au, Ag, Cu, Ni, Co and many others) can be deposited within the pores of an AAO template and hence in this method organic nanowires can be easily interfaced with a metal electrode with an appropriate work function suitable for device applications. Later in this work we will discuss the transport properties of Co-organic axially heterostructured bilayer nanowires.

2.2. XRD Characterization

To investigate the crystallinity of the as-grown nanowires, low angle XRD data has been acquired for the organic nanowire arrays hosted in the anodic alumina matrix. For this study the top surface of the sample is repeatedly cleaned by an appropriate organic solvent (as described before) to remove any residual thin film layer and then the nanowire tips are exposed by partial etching of the template in 5% phosphoric acid. **Figure 3** shows the typical LAXRD diffractograms observed for the following samples: (i) as grown (unannealed) rubrene nanowires, (ii) annealed rubrene and Alq_3 nanowires and (iii) blank alumina template with same thermal history as of (ii). Absence of any diffraction peaks indicates amorphous nature of the as-grown rubrene nanowires. The host alumina matrix does not exhibit any observable peak either in the scan range employed (Figure 3). This is in agreement

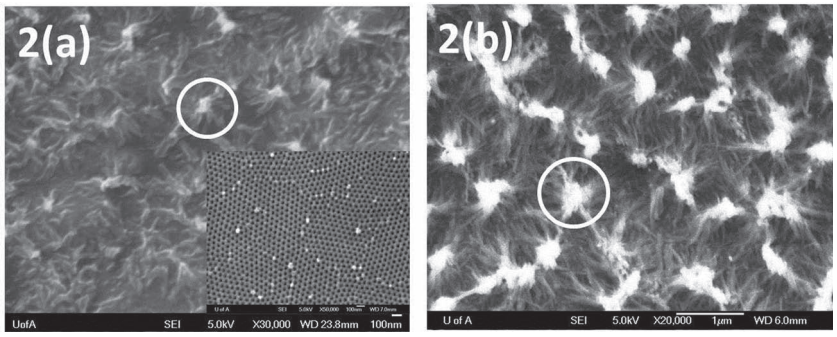

Figure 2. a) (inset) Empty AAO template with nominal pore diameter of 20 nm and wall thickness of 20 nm. (main image) Rubrene nanowires released from the template. b) Alq_3 nanowires released from the template. In (a,b), the nanowires coalesce together due to the removal of the host AAO matrix, as shown by the circles.

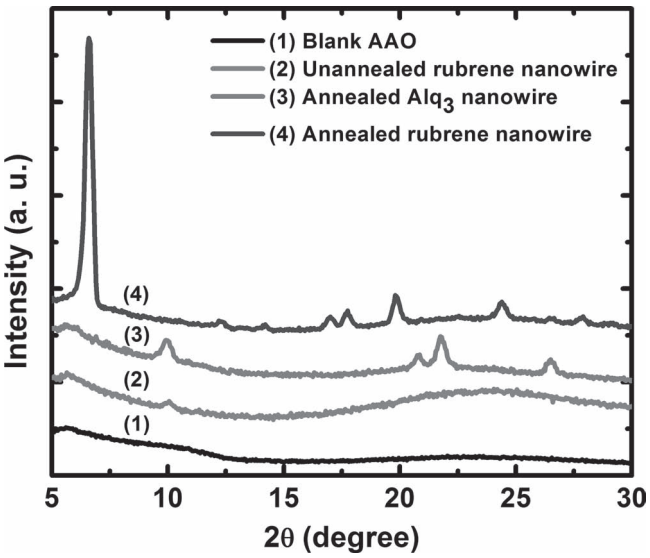

Figure 3. Low-angle X-ray diffractogram of organic nanowires and the host AAO template. The figure illustrates the effect of the annealing process on the crystallinity of the organic nanowires. Unannealed samples do not exhibit any peak, whereas annealed samples show signs of crystallinity and presence of new peaks.

with prior studies such as ref. [29–31]. However, the crystallinity of rubrene nanowires is significantly improved even after short time (~15 min) annealing at moderate temperature of ~200 °C. Similar behavior has been observed for other organic nanowires as well. Further optimization of the annealing parameters may result in better crystallinity of the organic nanowires.

The peak positions and relative intensities of rubrene nanowires (Figure 3, post annealing) have close resemblance with those observed for single crystal rubrene and wide rubrene nanowires (~200 nm diameter) grown by physical vapor transport.[37] For single crystal rubrene a very sharp crystalline peak occurs at $2\theta \approx 6.7°$ which originates from the (002) plane. This agrees well with Figure 3 and indicates strong π–π stacking along the *b* axis and high degree of crystallinity along the *a*-*b* plane for the rubrene nanowires.[37] We note that rubrene nanowires grown by physical vapor transport exhibit much weaker response at this angle and indicates lower degree of crystallinity.[37]

The rest of the peaks for single crystal rubrene occur at 2θ values 12°, 14°, 20° and 27°, which correspond to (010), (004), (006) and (008) planes respectively.[37] These peaks are also present in the XRD spectrum of our nanowire structures.

Two additional peaks in the nanowire XRD spectrum (Figure 3) occur at 2θ values 17° and 24°, which represent (300) and (020) planes, respectively. Similar peaks (albeit weaker) have been reported earlier[37] and was attributed to constrained growth of the organic nanowire within limited space of the pore. The presence of these additional peaks provides strong evidence of nanowire formation.

In our pattern we observe another new peak at ~18° (2θ) which may originate from enhanced space constraints imposed by smaller diameter pores. We note that there are two major differences between our rubrene nanowire and the vapor phase grown nanowires.[37] First, the former is essentially a solution-based method whereas the latter employs physical vapor transport as the growth mode. The second difference lies in the geometry of the nanowires. As discussed before, our nanowires are approximately 1 μm long with 50-70 nm diameter whereas the nanowires reported in ref. [37] are 50 μm in length with 200 nm diameter. These factors can lead to different molecular packing within the pores and hence different diffraction peaks. Nevertheless the presence of the characteristic peaks in the LAXRD pattern confirms the growth and high degree of crystallinity of rubrene nanowires within the AAO templates.

Similarly for Alq_3 nanowires we observe characteristic peaks at $2\theta \approx 10°$, 21°, 22° and 27° (Figure 3), which are consistent with previously reported data.[47] No peaks have been observed in the 2θ range 13°–18°. Further optimization of the annealing parameters is expected to improve the molecular arrangements.

2.3. FTIR and PL Characterization

The tips of the organic nanowires near the top-surface of the template are exposed to ambient air and are therefore prone to oxidation.[48] The nanowire tips at the bottom surface are however protected by the host alumina matrix, if the barrier layer is not removed. To examine the bonds in as-grown unoxidized organic nanowires, we have therefore performed attenuated total reflection (ATR) Fourier transform infrared (FTIR) measurements on the nanowire/barrier layer interface (to a depth > 50 nm, much larger than barrier layer thickness of 10–30 nm) in the mid-infrared regime and have compared the data with bulk organic powder. To prepare such samples we protected the top surface of the nanowires by a polymer coating and then the aluminum substrate was dissolved in a mercuric chloride solution. The organic nanowires were never in direct contact with this etchant and effect of such contaminants is therefore minimized in the FTIR response.

Figure 4a,b show the representative results obtained from rubrene and Alq_3 nanowires at room temperature. The data has been acquired after subtracting the background response originating from ambient air and host alumina template. For rubrene nanowires (Figure 4a), the characteristic peaks have close resemblance with rubrene crystal and powder reported before.[49,50] The three closely spaced peaks at ~3000 cm^{-1} are typically associated with C-H bond stretching[49] (Scheme 1) and are present in both powder and nanowire spectra. The remaining peaks originate from the skeletal vibration of ring (Scheme 1) and are also present in both spectra.

Figure 4b shows the FTIR spectra for Alq_3 nanowires (annealed and unannealed) and bulk powder. Interestingly, the bulk vibrational modes (in the range ~1250–1750 cm^{-1}, commonly associated with ring stretching, CH bending vibrations of the ligands, CN stretching and CO stretching,[51] and in the range ~2800–3000 cm^{-1}, associated with CH stretching, see scheme 1) are greatly suppressed in unannealed nanowires, although a band at ~1000 cm^{-1} is observed which is related to Al-N stretching. Similar observation has been made before[18] where Alq_3 nanoclusters show significantly less motional modes compared to bulk.

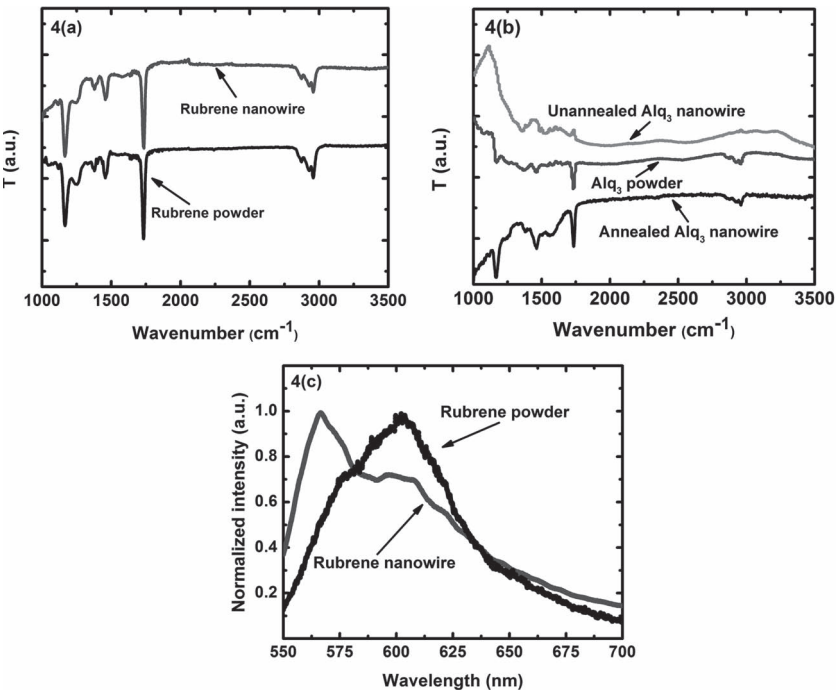

Figure 4. a,b) FTIR transmission spectra for rubrene and Alq_3 powder and nanowires in the mid-infrared regime. c) Photoluminescence spectra for rubrene powder and nanowires. All data were acquired at room temperature.

To investigate if the disordered nature of the organic is contributing to the observed difference, we have performed FTIR measurements on annealed Alq_3 nanowire samples. Annealing condition is the same as in the XRD experiments discussed before. Annealing has been found to modify the FTIR response (Figure 4b) and after annealing the peaks coincide with the Alq_3 powder sample. This indicates that there is some correlation between local disorder (which is reduced after annealing) and the FTIR spectrum. Also, annealing may remove some volatile organic impurities, which can also be a reason for this improvement. This also indicates that the FTIR signal is unlikely to originate from any foreign entities (e.g. contamination from oxygen/moisture/mercuric chloride) in the nanowire since such states are generally immune to annealing. We note that similar effects have been reported in other studies such as ref. [52,53].

However, even after annealing, the spectrum does not match perfectly with the powder, especially in the lower wavenumber regime where a monotonically decreasing trend is superimposed on the peaks. Such differences can originate from the substrate-effect due to the presence of the alumina host or different structural organization of the organic molecules within the nanopores.[54]

Figure 4c shows the photoluminescence (PL) spectrum (excitation wavelength 532 nm) obtained from rubrene nanowires and bulk powder at room temperature. For nanowire samples, the main peak appears at ~570 nm (which corresponds to photon energy of ~2.1 eV and the HOMO-LUMO gap of rubrene) and a shoulder peak occurs at ~600 nm. This agrees well with the PL spectra of single crystal rubrene[37,48,50] and organic vapor transport grown nanowire rubrene[37] reported before. For bulk powder, the main peak shifts at a higher wavelength (~600 nm) due to oxidation of rubrene powder.[48,50]

2.4. Charge Transport Measurements

To investigate the nature of charge transport in the nanowire organic, we have conducted variable temperature current-voltage (I–V) measurements in a vertical geometry. **Figure 5** shows measurement results from PCBM and rubrene nanowires. Data from other organics exhibit qualitatively similar behavior. The measurements have been performed in the dark with sample temperature varying from 8 K to 300 K. Figure 5a shows the device schematic and FESEM image of axially heterostructured bilayer Co-rubrene nanowires. In vertical geometry, multiple nanowires are connected in parallel between the top and bottom contacts. Since the top contact area is ~1 mm^2 we estimate ~10^8 nanowires are connected in parallel (pore density estimated from Figure 1a, bottom inset). The equivalent circuit for the measurement set up is shown in Figure 5a. We note that some "averaging effect" is unavoidable in the vertical configuration. Nevertheless, previous studies on vertical configurations have shown that if the nanowires are nominally identical then multi-nanowire devices exhibit qualitatively same behavior as planar single nanowire devices.[55,56] Further, vertical geometry avoids any chemical doping of the organic nanowires that invariably occurs during the chemical treatment steps required for releasing the nanowires from the AAO host matrix. Parallel array of nanowires are also desirable from a device perspective where large drive current is required.

The blank template (not bearing any organic) exhibits extremely high resistance for same contact area, which is beyond the measurement capability of our equipment. As determined from the control experiments, the resistance of the contacts (bottom cobalt nanowire and top nickel film) is much less than that of the organic nanowires and shows Ohmic I–V characteristics with a temperature-dependence same as metals. Thus the characteristics discussed below originate from the organic nanowires (see the equivalent circuit in Figure 5a).

Figure 5b shows the I–V characteristics of PCBM nanowires. The characteristics are symmetric in the bias range [–0.5, 0.5 V] and do not show any rectification effect. This can be attributed to similar coupling with the top and bottom contacts (Ni and Co). For PCBM nanowires, I–V characteristics are non-linear at low temperature (<50 K) and become increasingly linear with concomitant reduction in resistance (obtained from $\left({}^{dI}/_{dV}\right)^{-1}$) as the temperature is increased (50–200 K). This indicates that the organic nanowire has a non-metallic behavior and, combined with the disordered nature of these systems as observed previously from the XRD data, suggests hopping as the dominant

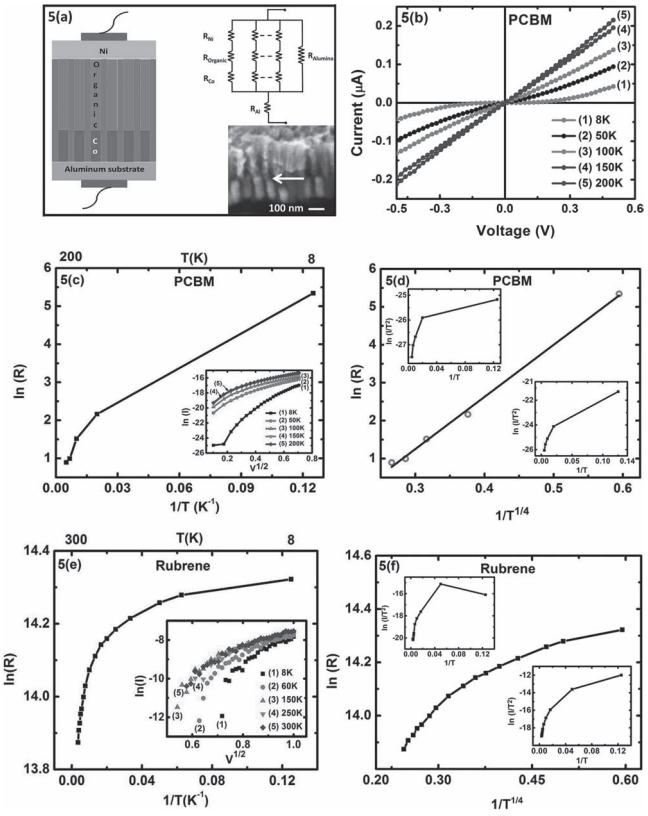

Figure 5. a) (left) Device schematic in the vertical geometry and (bottom right) FESEM image of Co-Rubrene bilayerd nanowire. The arrow indicates the heterointerface. (top right) Corresponding equivalent circuit. b) Temperature-dependent current-voltage characteristics of PCBM nanowires. c) *ln* R vs. inverse temperature (1/*T*) for PCBM nanowires at low bias (0.1 V). The inset shows *ln* I versus $\sqrt{V}$ as a function of temperature. d) *ln* R versus $T^{-\frac{1}{4}}$ for same bias as in (c). The straight line shows a linear fit to the data. The insets show *ln* (I/T^2) as a function of inverse temperature (1/*T*) for two different bias values (top inset: 0.1 V, bottom inset: 0.5 V). e) *ln* R vs. 1/*T* plot for rubrene nanowires at low bias (0.5 V). The inset shows *ln I* versus $\sqrt{V}$ at various temperatures. f) *ln* R versus $T^{-\frac{1}{4}}$ for same bias as in (e). The insets show *ln* (I/T^2) as a function of inverse temperature (1/*T*) for two different bias values (top inset: 0.5 V, bottom inset: 1 V).

transport mechanism.[55,57,58] Using the FESEM data we estimate wire diameter ~70 nm, wire length ~500 nm, and calculate the resistivity (ρ) of the PCBM nanowire to be ~8 MΩ-m at 200 K. The extracted resistivity data indicates that the nanowires are most likely unintentionally doped due to exposure of the top surface to air. Non-linearity in the *I-V* characteristics at low temperature and high bias (Figure 5b) often occurs in organic systems and is a signature of electric field induced hopping.[55] Figure 5c shows *ln* R vs. inverse temperature plot. At lower temperature (<50 K), thermal energy fails to sustain hopping and the resistance tends to saturate in this temperature regime. Tunneling between impurity states is most likely the dominant conduction mechanism in this range.[55,58]

Temperature dependent transport in disordered organic is usually understood in the framework of Mott's variable range hopping theory (instead of band transport that is applicable for ordered solids).[57] According to Mott's theory, resistance $R(T) \propto \exp\left[\left(\frac{T_0}{T}\right)^{\gamma}\right]$ where the parameter γ is related to the dimensionality (d) of the conducting medium by the relation $\gamma = 1/(1+d)$ (d = 1, 2 and 3 for one, two and three dimensional system, respectively).[55,57] In this model T_0 is the Mott temperature that depends on the electronic structure of the conducting medium.[55] The best linear fit to our *ln* (R) vs. $1/T_{\gamma}$ data has been obtained for $\gamma = 1/4$ (or, $d = 3$) as shown in Figure 5d. This indicates that three-dimensional (d = 3) variable range hopping is the appropriate transport model for the PCBM nanowires. To investigate the contribution of the metal/PCBM nanowire interface in the total device resistance, we have plotted *ln* (I) versus $V^{1/2}$ for different temperatures (Figure 5c inset) and *ln* (I/T^2) versus $1/T$ for two different bias values (Figure 5d, insets).[55,58] Absence of linearity in these plots indicates that tunnel injection at the interface or thermionic emission over Schottky barrier is not the dominant process in our samples.[55,58]

For rubrene nanowires, the *I–V* characteristics remain nonlinear and symmetric at all temperatures (not shown). Figure 5e shows typical *ln* R vs $1/T$ data for rubrene nanowire samples. Again, as observed before, the resistance saturates in the lower temperature regime. The *ln* (R) vs. $1/T^{1/4}$ plot (Figure 5f) is quasi-linear, indicating that transport mechanism cannot be fully captured within the framework of three-dimensional variable range hopping. This indicates inapplicability of the assumptions that are inherent in Mott's variable range hopping theory for these systems. For example, the assumption of constant density of states near the Fermi energy may not be valid in a highly disordered system.[59] It is possible to have a Gaussian or exponential distribution of the hopping states or a Coulomb gap near the Fermi level, which will significantly affect transport properties and introduce deviations from the Mott's model.[59] A detailed investigation of the trap states is however beyond the scope of this paper. Other factors that can potentially affect the concentration of mobile carriers and the transport characteristics include incomplete ionization, formation of complexes and presence of trap states in the host alumina. The insets of Figure 5e,f confirm that transport in rubrene nanowire devices is not limited by charge injection at the interfaces.[55,58]

Another fabrication step that can introduce additional traps and affect transport results is the e-beam deposition of the top metallic contact on organic. It is known that during deposition of the top contact in a vertical geometry (as shown in Figure 5a), ferromagnetic atoms or clusters tend to penetrate "soft" organic and create a disordered and ill-defined interface.[60–62] These atoms and clusters form complexes with the organic and introduce additional trap levels within the HOMO-LUMO gap. In our XRD and FTIR samples no top contact was present so those results are not affected by this effect. To improve the top metal/organic interface, a buffer layer can be deposited on top of the organic before metal deposition. This layer could be a tunnel barrier made of alumina or lithium fluoride.[63] Another option is to use substrate-cooling during deposition of the top metal contact.[64]

2.5. Magnetotransport Measurements

We also investigate the magnetotransport properties of the as-synthesized organic nanowires since organic systems often

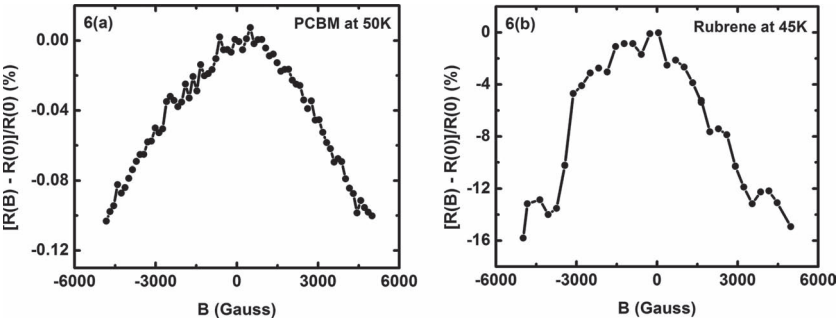

Figure 6. Low temperature negative magnetoresistance response of a) PCBM nanowires and b) rubrene nanowires, measured in vertical geometry.

exhibit "organic magnetoresistance" (OMAR) effect, which has recently attracted significant attention due to both fundamental physics[65,66] and sensor applications.[67] As discussed above, carrier transport in disordered organic nanowires occurs via hopping. It is well-known that in presence of an external magnetic field variable range hopping results in a positive magnetoresistance.[55] This mechanism, commonly known as the "wavefunction shrinkage model,"[55] is due to the fact that spatial extent of the electron wavefunction "shrinks" in presence of a magnetic field. This lowers the wavefunction overlap between the localized states and reduces the hopping probability. As a result, device resistance increases with increasing magnetic field. **Figure 6** shows representative magnetoresistance plots for rubrene and PCBM nanowires. We note that in our samples, a negative magnetoresistance is observed. This effect cannot be explained within the framework of the wavefunction-shrinkage model[55] as described above. Such negative magnetoresistance is however consistent with the OMAR effect, which has been recently discovered in planar organic devices.[65–67]

The origin of OMAR is still a scientific puzzle.[65,66] However, experimental data indicate that hyperfine interaction (mainly originating from the hydrogen atoms in the organic) play a crucial role.[65,66] Spin-orbit interaction is weak in organics unless they are intentionally doped by heavy atoms[65] and hence spin-orbit interaction does not affect OMAR. Organics with weaker hyperfine interaction (fewer hydrogen atoms) have been found to exhibit weaker OMAR.[65,66] This is consistent with Figure 6, which shows that compared to PCBM nanowires, rubrene nanowires exhibit almost two orders of magnitude stronger OMAR response. This is expected since hydrogen atoms are more abundant in rubrene molecules compared to PCBM (Scheme 1), and hence stronger hyperfine interaction is expected in rubrene.

However, compared to previously reported thin film devices, nanowire samples show a much wider linewidth (or zero-field cone) in their magnetoresistance response and do not show any sign of saturation in the field range [-5, 5] kGauss. This indicates that the strength of the "characteristic magnetic field" (B_0),[65] responsible for the OMAR effect, is significantly different in nanowire samples compared to thin film devices. One possible origin of this effect is the three-dimensional molecular packing in the nanowire geometry,[17] which differs significantly from thin film or bulk, as observed from the structural characterizations described before.

3. Conclusion

In summary, we have developed a unique fixed-angle centrifugation-assisted growth process for high yield synthesis of organic molecular nanowires and have performed extensive material and device characterization. We demonstrate fabrication of nanowires of four different materials, which are commonly used in organic light emitting diodes, solar cells, thin film transistors and organic spin valve devices. The material set can be expanded to include other molecular organics, which can be dissolved in common organic solvents. We have also demonstrated fabrication of axially heterostructured metal-organic bilayer nanowires. We believe that this process can be applied to synthesize axially or radially heterostructured multilayer organic nanowires by optimizing fabrication parameters such as centrifugation speed, duration and concentration of the organic solution. All these devices, depending on their intended functionality, can be fabricated on arbitrary substrates such as (indium tin oxide coated) glass or silicon. The organic nanowires exhibit different crystal growth characteristics, modified motional modes, photoluminescence and negative OMAR, which can be exploited for molecular electronic, optical and spintronic devices based on these systems.

Supporting Information

Supporting Information is available from the Wiley Online Library or from the author.

Acknowledgements

This work was supported by the Disruptive Technology Challenge program (TRLabs, Canada), NanoBridge and NSERC, Canada. The authors would like to thank De-ann Rollings (Earth and Atmospheric Sciences Department, University of Alberta) and Shiraz Merali (Chemical and Materials Engineering, University of Alberta) for help in acquiring FESEM images and XRD characterization respectively.

Received: December 7, 2011
Revised: February 22, 2012
Published online: April 18, 2012

[1] S. Forrest, P. Burrows, M. Thompson, *IEEE Spectrum* **2000**, *37*, 29–34.
[2] S. R. Forrest, *Nature* **2004**, *428*, 911–918.
[3] G. Chidichimo, L. Filippelli, *Int. J. Photoenergy* **2010**, *2010*, 1–11.
[4] S. Günes, H. Neugebauer, N. S. Sariciftci, *Chem. Rev.* **2007**, *107*, 1324–1338.
[5] J. E. Slota, X. He, W. T. S. Huck, *Nano Today* **2010**, *5*, 231–242.
[6] M. D. Kelzenberg, D. B. Turner-Evans, M. C. Putnam, S. W. Boettcher, R. M. Briggs, J. Y. Baek, N. S. Lewis, H. A. Atwater, *Energy Environ. Sci.* **2011**, *4*, 866–871.
[7] M. Aryal, F. Buyukserin, K. Mielczarek, X.-M. Zhao, J. Gao, A. Zakhidov, W. Hu, *J. Vac. Sci. Technol. B* **2008**, *26*, 2562.
[8] N. Haberkorn, J. S. Gutmann, P. Theato, *ACS Nano* **2009**, *3*, 1415–1422.

[9] J. L. Duvail, Y. Long, S. Cuenot, Z. Chen, C. Gu, *Appl. Phys. Lett.* **2007**, *90*, 102114.
[10] A. L. Briseno, S. C. B. Mannsfeld, S. A. Jenekhe, Z. Bao, Y. Xia, *Mater. Today* **2008**, *11*, 38–47.
[11] V. A. Dediu, L. E. Hueso, I. Bergenti, C. Taliani, *Nat. Mater.* **2009**, *8*, 707–716.
[12] K. M. Alam, S. Pramanik, in *Nano-Semiconductors: Devices and Technology*, (Ed: K. Iniewski), CRC Press, Boca Raton, FL, **2012**, Ch. 4.
[13] W. J. M. Naber, S. Faez, W. G. van der Wiel, *J. Phys. D* **2007**, *40*, R205–R228.
[14] S. Pramanik, C.-G. Stefanita, S. Patibandla, S. Bandyopadhyay, K. Garre, N. Harth, M. Cahay, *Nat. Nanotechnol.* **2007**, *2*, 216–219.
[15] B. Kanchibotla, S. Pramanik, S. Bandyopadhyay, M. Cahay, *Phys. Rev. B* **2008**, *78*, 193306.
[16] T. D. Nguyen, G. Hukic-Markosian, F. Wang, L. Wojcik, X.-G. Li, E. Ehrenfreund, Z. V. Vardeny, *Nat. Mater.* **2010**, *9*, 345–352.
[17] Z. G. Yu, *Phys. Rev. Lett.* **2011**, *106*, 106602.
[18] L. Das, J. Mateo, S. Bandyopadhyay, S. Bandyopadhyay, J. Edwards, J. Anderson, *Appl. Phys. Lett.* **2011**, *98*, 063109.
[19] K. M. Alam, S. Pramanik, *Phys. Rev. B* **2011**, *83*, 245206.
[20] F. S. Kim, G. Ren, S. A. Jenekhe, *Chem. Mater.* **2010**, *23*, 682–732.
[21] a) B. Kanchibotla, S. Pramanik, S. Bandyopadhyay, in *Nano and Molecular Electronics Handbook*, (Ed: S. E. Lyshevski), CRC Press, Boca Raton, FL, **2007**, Ch. 9; b) K. M. Alam, A. P. Singh, S. C. Bodepudi, S. Pramanik, *Surface Science* **2011**, *605*, 441.
[22] K. Kim, J.-I. Jin, *Nano Lett.* **2001**, *1*, 631–636.
[23] J. Joo, B. H. Kim, D. H. Park, H. S. Kim, D. S. Seo, J. H. Shim, S. J. Lee, K. S. Ryu, K. Kim, J.-I. Jin, T. J. Lee, C. J. Lee, *Synth. Met.* **2005**, *153*, 313–316.
[24] Y. Berdichevsky, Y. H. Lo, *Adv. Mater.* **2006**, *18*, 122–125.
[25] L. Zhang, F. Meng, Y. Chen, J. Liu, Y. Sun, T. Luo, M. Li, J. Liu, *Sens. Actuators B* **2009**, *142*, 204–209.
[26] S. I. Cho, W. J. Kwon, S.-J. Choi, P. Kim, S.-A Park, J. Kim, S. J. Son, R. Xiao, S.-H Kim, S. B. Lee, *Adv. Mater.* **2005**, *17*, 171–175.
[27] D. O'Carroll, I. Lieberwirth, G. Redmond, *Nat. Nanotechnol.* **2007**, *2*, 180–184.
[28] D. O'Carroll, D. Iacopino, A. O'Riordan, P. Lovera, É. O'Connor, G. A. O'Brien, G. Redmond, *Adv. Mater.* **2008**, *20*, 42–48.
[29] D. O' Carroll, J. Irwin, D. A. Tanner, G. Redmond, *Mater. Sci. Eng. B* **2008**, *147*, 298–302.
[30] G. A. O'Brien, A. J. Quinn, D. A. Tanner, G. Redmond, *Adv. Mater.* **2006**, *18*, 2379–2383.
[31] S. Moynihan, D. Iacopino, D. O'Carroll, P. Lovera, G. Redmond, *Chem. Mater.* **2011**, *20*, 996–1003.
[32] J. S. Kim, Y. Park, D. Y. Lee, J. H. Lee, J. H. Park, J. K. Kim, K. Cho, *Adv. Funct. Mater.* **2010**, *20*, 540–545.
[33] K. M. Coakley, B. S. Srinivasan, J. M. Ziebarth, C. Goh, Y. Liu, M. D. McGehee, *Adv. Funct. Mater.* **2005**, *15*, 1927–1932.
[34] D. H. Park, B. H. Kim, M. G. Jang, K. Y. Bae, J. Joo, *Appl. Phys. Lett.* **2005**, *86*, 113116.
[35] R. O. Al-Kaysi, T. H. Ghaddar, G. Guirado, *J. Nanomater.* **2009**, *2009*, 1–14.
[36] S. Pramanik, S. Bandyopadhyay, K. Garre, M. Cahay, *Phys. Rev. B* **2006**, *74*, 235329.
[37] J. W. Lee, K. Kim, D. H. Park, M. Y. Cho, Y. B. Lee, J. S. Jung, D. Kim, J. Kim, J. Joo, *Adv. Funct. Mater.* **2009**, *19*, 704–710.
[38] H. Liu, Y. Li, L. Jiang, H. Luo, S. Xiao, H. Fang, H. Li, D. Zhu, D. Yu, J. Xu, B. Xiang, *J. Am. Chem. Soc.* **2002**, *124*, 13370–13371.
[39] Y. J. Xing, G. Y. Jing, J. Xu, D. P. Yu, H. B. Liu, Y. L. Li, *Appl. Phys. Lett.* **2005**, *87*, 263117.
[40] H. Gan, H. Liu, Y. Li, L. Gan, L. Jiang, T. Jiu, N. Wang, X. He, D. Zhu, *Carbon* **2005**, *43*, 205–208.
[41] T. A. Beierlein, B. Ruhstaller, D. J. Gundlach, H. Riel, S. Karg, C. Rost, W. Rieß, *Synth. Met.* **2003**, *138*, 213–221.
[42] J. Mei, M. Bradley, V. Bulović, *Phys. Rev. B* **2009**, *79*, 235205.
[43] T. R. B. Foong, A. Sellinger, X. Hu, *ACS Nano* **2008**, *2*, 2250–2256.
[44] J. J. Hill, K. Haller, K. J. Ziegler, *J. Electrochem. Soc.* **2011**, *158*, E1-E7.
[45] N. Taşaltın, S. Öztürk, N. Kılınç, H. Yüzer, Z. Z. Öztürk, *Appl. Phys. A* **2009**, *95*, 781–787.
[46] K. H. Lee, C. C. Wong, *J. Appl. Phys.* **2009**, *106*, 104305.
[47] Chang-Jie Mao, Dan-Chen Wang, Hong-Cheng Pan, Jun-Jie Zhu, *Ultrason. Sonochem.* **2011**, *18*, 473–476.
[48] C. Kloc, K. J. Tan, M. L. Toh, K. K. Zhang, Y. P. Xu, *Appl. Phys. A* **2008**, *95*, 219–224.
[49] P. Zhang, X. Zeng, J. Deng, K. Huang, F. Bao, Y. Qiu, K. Xu, J. Zhang, *Jpn. J. Appl. Phys.* **2010**, *49*, 095501.
[50] K. K. Zhang, K. Tan, C. Zou, M. Wikberg, L. E. McNeil, S. G. Mhaisalkar, C. Kloc, *Org. Electron.* **2010**, *11*, 1928–1934.
[51] Y. Sakurai, Y. Hosoi, H. Ishii, Y. Ouchi, G. Salvan, A. Kobitski, T. Kampen, D. Zahn, K. Seki, *J. Appl. Phys.* **2004**, *96*, 5534.
[52] R. J. Curry, W. P. Gillin, J. Clarkson, D. N. Batchelder, *J. Appl. Phys.* **2002**, *92*, 1902–1905.
[53] W. H. Kim, G. P. Kushto, H. Kim, Z. H. Kafafi, *J. Polym. Sci. Part B: Polym. Phys.* **2003**, *41*, 2522–2528.
[54] G. Srinivasan, M. Pursch, L. C. Sander, K. Müller, *Langmuir* **2004**, *20*, 1746–1752.
[55] L. Gence, S. Faniel, C. Gustin, S. Melinte, V. Bayot, V. Callegari, O. Reynes, S. Demoustier-Champagne, *Phys. Rev. B* **2007**, *76*, 115415.
[56] L. Gence, V. Callegari, S. Faniel, A. Vlad, C. Dutu, S. Melinte, S. Demoustier-Champagne, V. Bayot, *Phys. Status Solidi (a)* **2008**, *205*, 1447–1450.
[57] S. N. F. Mott, *Conduction in Non-crystalline Materials*, Oxford University Press, Oxford **1987**.
[58] J. C. Scott, *J. Vac. Sci. Technol. A* **2003**, *21*, 521.
[59] G. Paasch, T. Lindner, S. Scheinert, *Synth. Met.* **2002**, *132*, 97–104.
[60] Y. Q. Zhan, M. P. de Jong, F. H. Li, V. Dediu, M. Fahlman, W. R. Salaneck, *Phys. Rev. B* **2008**, *78*, 045208.
[61] H. Vinzelberg, J. Schumann, D. Elefant, R. B. Gangineni, J. Thomas, B. Büchner, *J. Appl. Phys.* **2008**, *103*, 093720.
[62] W. Xu, J. Brauer, G. Szulczewski, M. Sky Driver, A. N. Caruso, *Appl. Phys. Lett.* **2009**, *94*, 233302.
[63] V. Dediu, L. E. Hueso, I. Bergenti, A. Riminucci, F. Borgatti, P. Graziosi, C. Newby, F. Casoli, M. P. De Jong, C. Taliani, Y. Zhan, *Phys. Rev. B* **2008**, *78*, 115203.
[64] Y. Liu, S. M. Watson, T. Lee, J. M. Gorham, H. E. Katz, J. A. Borchers, H. D. Fairbrother, D. H. Reich, *Phys. Rev. B* **2009**, *79*, 075312.
[65] T. Nguyen, Y. Sheng, J. Rybicki, G. Veeraraghavan, M. Wohlgenannt, *J. Mater. Chem.* **2007**, *17*, 1995.
[66] T. D. Nguyen, Y. Sheng, M. Wohlgenannt, T. D. Anthopoulos, *Synth. Met.* **2007**, *157*, 930–934.
[67] G. Veeraraghavan, T. D. Nguyen, Yugang Sheng, O. Mermer, M. Wohlgenannt, *IEEE Trans. Electron Dev.* **2007**, *54*, 1571–1577.